

Differential rotation of the halo traced by the K-giant stars

HAO TIAN ¹
(LAMOST FELLOW)

CHAO LIU ¹

—
YOU GANG WANG ²

—
YAN XU ³

—
CHENGQUN YANG ³

—
BO ZHANG ⁴
(LAMOST FELLOW)

—
XIANG-XIANG XUE ³

¹Key Laboratory of Space Astronomy and Technology, National Astronomical Observatories, Chinese Academy of Sciences, Beijing 100101, PR China;

²Key Laboratory of Computational Astrophysics, National Astronomical Observatories, Chinese Academy of Sciences, Beijing, 100101 PR China

³Key Laboratory of Optical Astronomy, National Astronomical Observatories, Chinese Academy of Sciences, Beijing 100101, PR China;

⁴Department of Astronomy, Beijing Normal University, Beijing 100875, PR China

(Received June 1, 2019; Revised January 10, 2019; Accepted July 3, 2020)

Submitted to ApJ

ABSTRACT

We use K-giant stars selected from the LAMOST DR5 to study the variation of the rotational velocity of the galactic halo at different space positions. Modelling the rotational velocity distribution with both the halo and disk components, we find that the rotational velocity of the halo population decreases almost linearly with increasing vertical distance to the galactic disk plane, Z , at fixed galactocentric radius, R . The samples are separated into two parts with $6 < R < 12$ kpc and $12 < R < 20$ kpc. We derive that the decreasing rates along Z for the two subsamples are -3.07 ± 0.63 and -1.89 ± 0.37 km s^{-1} kpc $^{-1}$, respectively. Compared with the TNG simulations, we suggest that this trend is probably caused by the interaction between the disk and halo. The results from the simulations show that only the oblate halo can provide a decreasing rotational velocity with an increasing Z . This indicates that the Galactic halo is oblate with galactocentric radius $R < 20$ kpc. On the other hand, the flaring of the disk component (mainly the thick disk) is clearly traced by this study, with R between 12 and 20 kpc, the disk can vertically extend to $6 \sim 10$ kpc above the disk plane. What is more interesting is that, we find the Gaia-Enceladus-Sausage (GES) component has a significant contribution only in the

halo with $R < 12$ kpc, i.e. a fraction of 23–47%. While in the outer subsample, the contribution is too low to be well constrained.

Keywords: galaxies: individual (Milky Way) — Galaxy: halo — Galaxy: kinematics and dynamics

1. INTRODUCTION

The stellar halo is one of the most important components in the Milky Way. Under the paradigm of Λ cold dark matter model, the halo is formed through accretion and merging the satellites, and plenty of substructures are supposed to be left in the halo. So the halo has been recording the information of the formation history. As a result, studies on the stellar halo can directly help us understand the formation our Milky Way. But the stellar halo is the most difficult component to be studied. The halo is quite diffused and of low density, and it can reach out to the volumes as far as more than 100 kpc (Bland-Hawthorn & Gerhard 2016, also references there). That means it is hard to obtain the velocity information, i.g. proper motions and radial velocities. What is more, the distance is also difficult to be well determined, except the standard candles like RR Lyrae stars or the blue horizontal branch stars (Xue et al. 2008; Hernitschek et al. 2018; Thomas et al. 2018). That brings the main difficulty to obtain a sufficient sample of tracers to study the properties of the stellar halo.

Thanks to the fast development of large survey projects, e.g. the Sloan Digital Sky Survey (SDSS; York et al. 2000), the Panoramic Survey Telescope and Rapid Response System (Pan-STARRS; Bernard et al. 2016) and Gaia mission (Gaia Collaboration et al. 2016, 2018a), many of those embedded substructures have been discovered in the halo, e.g. the Sagittarius Stream (Ibata et al. 1994), GD-1 Stream (Grillmair & Dionatos 2006a,b) and the ω -Cen Stream (Ibata et al. 2019). Those substructures, especially those thin cold streams, are quite helpful for studying the halo profile. Lux et al. (2013) introduced a method using Markov Chain Monte Carlo technique to constrain the halo shape with thin streams. The streams NGC 5466 and Pal 5 are proved to be the best candidate according to their orbit properties. Sanderson et al. (2015) also studied how to constrain the halo profile with action distributions of streams. The results show that even for the simple case of spherical potential, at least 20 streams with more than 100 member stars are required to make sure the potential well constrained. With the most prominent stream, the Sagittarius Stream, Law & Majewski (2010) introduced a triaxial model, which can well reproduce the Sagittarius Stream. But there are still some points which are not consistent with observations in the following years after that (see Dierickx & Loeb 2017, and references mentioned there). Vera-Ciro & Helmi (2013) also studied the halo shape using the Sagittarius Stream with the effect of the Magellanic Clouds considered. Differently, their results suggested an oblate halo. According to all above, we can find that the streams are powerful tracers to constrain the halo profile.

Many direct efforts other than using tidal substructures are also made to profile the halo. Valluri et al. (2012) showed that the halo shape can be probed with the orbital properties of individual halo stars, e.g. the action and frequency. The results from the complementary simulations show that the disk plays an important role to the shape of the inner halo and making it oblate, but not for the outer part. Using the K-giant stars selected from the DR5 of the Guoshoujing Telescope (Large Sky Area Multi-Object Fiber Spectroscopic Telescope, LAMOST hereafter), Xu et al. (2018) showed a complicated halo, the profile is different for the inner and outer parts. Traced by the K-giant stars selected from the LAMOST DR5, the shape of the halo varies from oblate for the inner part to almost spherical for the outer part.

To figure out the interaction between different components in the Milky Way, we should do a deep analysis on the dynamics of the components. The second data release of Gaia mission (Gaia DR2, hereafter) contains proper motions and parallaxes for more than 1.3 billion stars, and radial velocities for stars brighter than 14 in G -band (Gaia Collaboration et al. 2018a). The accurate astrometric data greatly improves the study on the dynamics of the disk and the halo (Belokurov et al. 2019). The phase spiral signature in the local volume was discovered by Gaia Collaboration et al. (2018b) and Antoja et al. (2018) for the first time, which indicates a possible interaction between the satellite of the Milky Way and the disk (Laporte et al. 2019, Xu et al. in prep.). The spectroscopic surveys, including APOGEE and LAMOST, have brought a big progress during the study on the Milky Way. The combination of the APOGEE/LAMOST and the Gaia datasets provides a unique opportunity to study the formation of the halo. Combining the astrometric data Gaia DR2 and APOGEE, Helmi et al. (2018) revealed a major merger event in the local volume, named Gaia-Enceladus (also known as Gaia-Sausage, Belokurov et al. 2018). With the combination of spectroscopic survey LAMOST and Gaia DR2, Tian et al. (2019, hereafter Paper I) measured the halo rotational velocity of $V_T = +27_{-5}^{+4}$ km s⁻¹ of the halo in the solar neighbourhood using the K-giant sample.

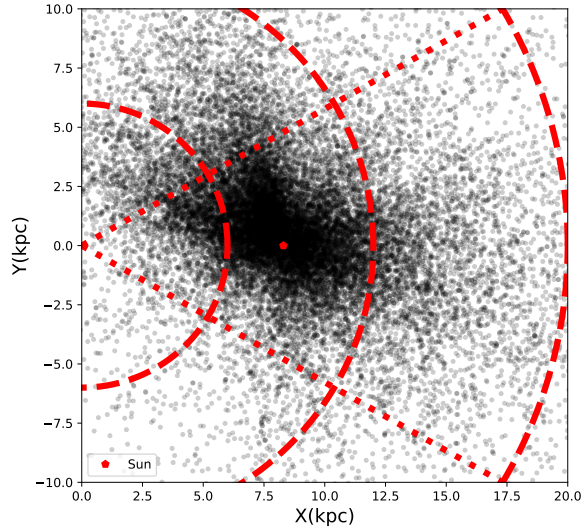


Figure 1. The space distribution of the K-giant sample is shown. The dashed and dotted lines represent the limits on θ and R in cylindrical frame, -30° and 30° for θ and 6, 12 and 20 kpc for R from inner to outer.

According to the studies by [Rodríguez-Gomez et al. \(2017\)](#), the morphology for the massive and dwarf galaxies significantly depends on the assemble history and spin, respectively. For the Milky Way-like galaxies, the morphology depends on a combination of the two factors. To figure out if the halo shape is related to the spin variance, similar with Paper I, we will also use the K-giant stars to do a further study on the rotation of the halo. The K-giant stars are perfect tracers for studying the dynamics of the halo. First, giant stars have higher luminosity, which is quite helpful to trace distant volumes. Second, the K-giant stars are of higher quantity which brings enough samples for statistics, especially for studies on the global properties of the stellar halo.

The LAMOST is a 4 meter, quasi-meridian, reflecting Schmidt telescope. There are 4000 fibers, which make it efficient to obtain spectra. The fifth data release (DR5) provides the radial velocity and metallicity for millions of stars with uncertainties of $\sim 5 \text{ km s}^{-1}$ and 0.1 dex respectively. The high efficiency helps LAMOST obtain more than 9 million spectra, which is the largest spectrum observation sample. Combined with Gaia DR2, it provides the unprecedented chance to study the Milky Way. More recently, the Seventh Data Release includes low- and medium-resolution spectra¹ of $R = 1800$ and 7500, respectively.

This paper is constructed as follows. In Section 2, we briefly introduce the dataset and the method. The results are shown in Section 3. The discussions are listed in Section 4.

2. DATA & METHOD

The same with Paper I, we still use the K-giant stars selected from LAMOST DR5 ([Liu et al. 2014](#)) to study the rotation velocities of the halo and thick disk in this paper. The LAMOST DR5 dataset provides the radial velocity and metallicity, with typical errors of $\sim 5 \text{ km s}^{-1}$ and 0.1 index, respectively. Following Paper I, we remove all the stars with metallicity $[\text{Fe}/\text{H}] > -1$ to reduce the contamination from disk, especially the thin disk stars (See Figure 4 in [Hayden et al. 2015](#)). That is proved to be quite efficient (as shown in Paper I). In this project, we aim at larger volumes, where the distances of the distant stars are no longer available from Gaia DR2. We adopt the distances provided by [Carlin et al. \(2015\)](#), which are estimated using the technique of Bayesian approach by comparing the stellar parameters and a grid of stellar isochrones with typical relative errors $\sim 20\%$.

To avoid systematic offset of the distances and radial velocities from LAMOST DR5 ([Tian et al. 2015](#); [Schönrich & Aumer 2017](#), and Paper I), we use the common stars of both LAMOST DR5 and Gaia DR2 to figure out the offset and correct the values from LAMOST DR5. The distance is normalized by 0.805 and the radial velocity is corrected

¹ <http://dr7.lamost.org/>

	Selection	f_H	V_ϕ^H	$\sigma_{V_\phi^H}$	f_D	V_ϕ^D	$\sigma_{V_\phi^D}$	f_{H^3}	$V_\phi^{H^3}$	$\sigma_{V_\phi^{H^3}}$	N
			km s ⁻¹	km s ⁻¹		km s ⁻¹	km s ⁻¹		km s ⁻¹	km s ⁻¹	
S	$-1 < Z < 1$	$0.70^{+0.04}_{-0.04}$	37^{+7}_{-7}	75^{+4}_{-4}	0.30	185^{+5}_{-5}	41^{+3}_{-3}	-	-	-	2215
	$1 < Z < 2$	$0.81^{+0.04}_{-0.05}$	50^{+5}_{-6}	79^{+3}_{-4}	0.19	177^{+5}_{-6}	38^{+4}_{-4}	-	-	-	2268
	$2 < Z < 4$	0.12	-18^{+41}_{-64}	82^{+17}_{-16}	$0.41^{+0.06}_{-0.07}$	127^{+9}_{-9}	55^{+4}_{-4}	$0.47^{+0.09}_{-0.11}$	12^{+4}_{-4}	33^{+5}_{-7}	3415
	$4 < Z < 6$	$0.77^{+0.05}_{-0.09}$	40^{+6}_{-4}	73^{+3}_{-3}	-	-	-	0.23	6^{+7}_{-7}	18^{+16}_{-12}	1731
	$6 < Z < 10$	$0.68^{+0.05}_{-0.05}$	24^{+4}_{-4}	82^{+4}_{-3}	-	-	-	0.32	14^{+4}_{-5}	12^{+10}_{-8}	1327
	$10 < Z < 15$	1	10^{+4}_{-4}	63^{+3}_{-3}	-	-	-	-	-	-	496
SO	$-1 < Z < 1$	$0.60^{+0.04}_{-0.04}$	23^{+11}_{-10}	80^{+13}_{-12}	0.40	221^{+2}_{-3}	20^{+3}_{-3}	-	-	-	287
	$1 < Z < 2$	$0.86^{+0.03}_{-0.04}$	20^{+7}_{-6}	59^{+10}_{-7}	0.14	201^{+7}_{-10}	28^{+11}_{-8}	-	-	-	218
	$2 < Z < 4$	$0.92^{+0.02}_{-0.02}$	20^{+3}_{-3}	46^{+4}_{-4}	0.08	194^{+8}_{-14}	32^{+11}_{-6}	-	-	-	537
	$4 < Z < 6$	$0.95^{+0.01}_{-0.02}$	9^{+4}_{-4}	54^{+4}_{-4}	0.05	201^{+9}_{-17}	28^{+16}_{-8}	-	-	-	482
	$6 < Z < 10$	$0.97^{+0.01}_{-0.01}$	6^{+3}_{-3}	53^{+3}_{-3}	0.03	192^{+18}_{-26}	45^{+22}_{-17}	-	-	-	639
	$10 < Z < 15$	1	1^{+4}_{-4}	60^{+4}_{-4}	-	-	-	-	-	-	395

Table 1. The first column lists the selection for each subsample. The results, including fraction f , the rotational velocity $\langle V_\phi \rangle$ and dispersions σ_{V_ϕ} , from Bayesian Method for each component are listed. Symbols H , D and 3 denote the disk, halo and the third component, respectively. The last column lists the numbers of the K-giant stars in each sub-sample. The top and bottom parts list the information of the volumes in S-sample and SO-sample, respectively.

by adding ~ 5.38 km s⁻¹. More details for distance and radial velocity correction are described in Appendix A and B, respectively.

Proper motions of the K giant star samples are obtained by cross-matching with Gaia DR2, then the positions and velocities are calculated with Python package *Galpy* (Bovy 2015). The Solar motion relative to the Local Standard of Rest from Schönrich et al. (2010) is adopted, $(U_\odot, V_\odot, W_\odot) = (11.1, 12.24, 7.25)$ km s⁻¹.

In order to study the variance of the rotational velocity of the halo with different heights to the disk plane, a sufficient sample for each volume is required. In this way, we firstly focus on the volumes with $6 < R < 12$ kpc, $-30^\circ < \phi < 30^\circ$, and $-1 < Z < 15$ kpc in galactocentric centered cylindrical coordinates. We adopt the Solar location from Reid et al. (2014) with $(R, \phi, Z) = (8.3$ kpc, $0^\circ, 0$ kpc). Here we ignore the distance of the Sun to the disk plane, which is too small to make any difference to our results. To constrain the uncertainties, only those stars with signal to noise ratio higher than 10, radial velocity errors $\sigma_{RV} < 10$ km s⁻¹ and proper motion errors $(\sigma_{\mu_\alpha}, \sigma_{\mu_\delta})$ smaller than 0.3 mas yr⁻¹ are used. This is labeled as the S-sample. A similar sample with different R range, $12 < R < 20$ kpc, is also selected for studying the outer part, labeled as SO-sample.

Along the height to the disk plane, we divide each of the two samples into 6 sub-volumes to make sure each sub-volume contains enough number of stars. The information for each sub-volume is listed in Table 1. The numbers of stars in each sub-volume are listed in the last column.

In Paper I, a Bayesian model including three Gaussian components was used for the local volume, the halo, the thick disk and a possible retrogradely rotating component. In this paper, we adopt the same method that includes the halo, the thick disk and a possible additional component. The Gaussian distribution of each component can be written as follow:

$$p_i(V_\phi^{(k)} | f_i, V_{\phi,i}, \sigma_i, \epsilon^{(k)}) = \frac{f_i}{\sqrt{2\pi(\sigma_i^2 + \epsilon_k^2)}} \exp\left(-\frac{(V_\phi^k - V_{\phi,i})^2}{2(\sigma_i^2 + \epsilon_k^2)}\right), \quad (1)$$

where $V_{\phi,i}$ and σ_i are the rotational velocity and its dispersion of the i th component, f_i is the number fraction of the i th component. V_ϕ^k and ϵ_k are the rotational velocity and its uncertainty of the k th star in cylindrical coordinates. Considering that the errors of the rotational velocity will be larger for distant stars, which may affect results, here we use the probability calculation with uncertainties involved, as shown in Equation 1. To determine the rotational velocities of the three components, the Python package *emcee* is applied on samples with different space selections as listed in Table 1. Affine solver is used with 50 walkers and 6000 iterations in total, including 3000 burn-in iterations. Trying to find the best-fit parameters with the components, we test models with different numbers of components, e.g. 1, 2 or 3 components according to the results mentioned in Paper I. The median values are adopted for each of the parameters. The lower and upper uncertainties are determined with the differences between the median value and the 16% and 84% values. A typical result for the parameter determination is showed in the Section C. Due to the large

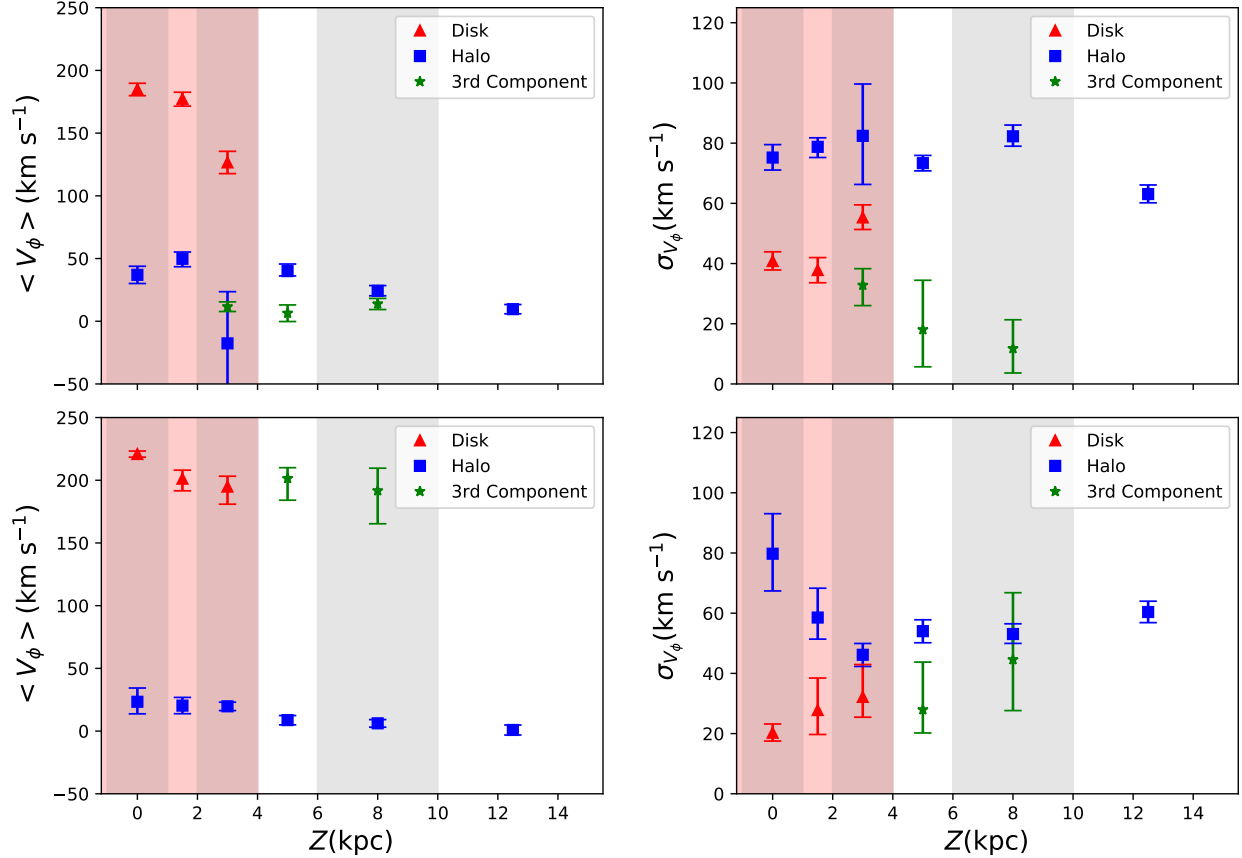


Figure 2. The distributions of the rotation velocity and its dispersion are shown in the left and right panels, respectively. The gray shadowed columns represent the bin range along Z . The red shadowed region represent the height lower than 4 kpc, where the disk component is always included in the Bayesian model. The top and bottom panels show the results from the S-sample and SO-sample, respectively. The blue and red symbols represent the parameters of the halo and disk components, respectively. The green ones represent the third component in the model. The errorbars represent the uncertainties of the values which are obtained from Markov chain Monte Carlo simulations.

contribution from the disk, the third component has low fraction in the lower volumes, especially in this paper, we have much lower number of stars in each volume than that in Paper I.

We find that the model with the disk and the halo components is better for volumes with $Z < 2$ kpc. As the contamination of the disk becomes lower for higher volume, i.e. $Z > 4$ kpc, the model with the halo and the retrogradely rotating components is better, rather than the halo and the disk. In general, the disk contributes very few stars ($\sim 8\%$) in those higher Z volumes ($Z = 5$ kpc) around $R = 9$ kpc (Wang et al. 2018). As a result, the contributions of the halo and the additional contribution will rise. In Table 1, for the transition volume with $2 < Z < 4$ kpc in S-sample, the disk contribution becomes weaker and the third component (the GES as described in the following section) increases. Then we constrain the parameters of a model with all the three components. This is not done for the volume with similar height in SO-sample because of the low number of the samples and the low contribution of the GES component (more discussion in the following sections). The median values are adopted as the best-fit parameters for each of the volume. The results for those space volumes are listed in Table 1. The markers H , D and 3 denote the halo, the disk and the third component, respectively.

3. RESULTS

Figure 2 represents the distributions of the rotational velocity and its dispersion in the left and right panels, respectively. The top and bottom panels are the results for S-sample and SO-sample, respectively. In each panel, the

parameters for the disk and halo components are represented by the red and blue symbols, respectively. The green ones show the parameters of the GES component in S-sample, or the extension of the disk in SO-sample.

3.1. Rotational velocity distribution of the halo

Focusing on the halo component, which is the main target in this paper, we find that the halo in S-sample (the blue symbols in Figure 2) is progradely rotating with rotational velocity dispersion around 75 km s^{-1} . The rotational velocity generally decreases versus the height to the disk plane. This is more clear in the left panel in Figure 3. The black solid line shows the linear fitting results, with rotational velocity uncertainties considered. The fitting results show that the decreasing rate is $-3.04 \pm 0.63 \text{ km s}^{-1} \text{ kpc}^{-1}$. The intercept of the line represents the rotational velocity of the halo at the disk plane, of $49 \pm 5.34 \text{ km s}^{-1}$. The volume with $2 < Z < 4 \text{ kpc}$ shows an exception of the variance. The uncertainties of the parameters are very large, that is because the fraction ($\sim 12\%$) of the halo is too low to be well constrained.

Different with the S-sample, the rotational velocity dispersion is no longer flat in the SO-sample, but decreases firstly and then keeps around a lower value, of 60 km s^{-1} . This is consistent with the variance of the rotational velocity dispersion showed by Bird et al. (2019).

Similar to the S-sample, the SO-sample also shows a decreasing trend of the rotational velocity of the halo. As showed in the right panel of Figure 3, the decreasing rate of the rotational velocity is lower than that of S-sample, of $-1.89 \pm 0.37 \text{ km s}^{-1} \text{ kpc}^{-1}$. The intercept of the fitting line is of $22.40 \pm 2.66 \text{ km s}^{-1}$. This is much lower than that of S-sample. That means the rotational velocity of the halo close to the disk plane is larger for the inner part.

3.2. The contribution of GES

The locations with $Z > 2 \text{ kpc}$ show a second halo component with low rotational velocity dispersion and close-to-zero rotational velocity (the green symbols in the top panels). This is consistent with the properties of the GES (Helmi et al. 2018; Belokurov et al. 2018; Myeong et al. 2019). It should be noticed that the GES component is not recognized in the lower volumes, that does not mean there is no contribution of the GES component in those volumes. The main reason is that the fraction of the GES member stars is too low to be well constrained at lower Z locations.

According to the distribution of the components, we calculate the probabilities of the components for each star. In this way, Figures 4 and 5 show the distributions of the stars in each volume color-coded by the probability to the disk component. Because the disk component is almost vanished in the higher volumes in S-sample, where there are only the halo and the GES components, we represent the probability of the GES in the subsample with $4 < Z < 6 \text{ kpc}$ (the top left panel in Figure 4).

GES is included in the Bayesian model as an independent component, because it has significantly different dynamical information with the halo (Helmi et al. 2018), smaller rotational velocity and dispersion and relatively larger energy. As showed in Figures 4 and 5, the probability for the GES member stars are around 50% at most. That means it is quite difficult to select a pure sample to study its chemical information. In Figure 6, the metallicity distributions of the stars with probability higher or lower than 0.4 in S-sample with $4 < Z < 6 \text{ kpc}$ are showed. We find that the distribution with higher probabilities is still different with that from Helmi et al. (2018), because of the high contamination ($> 50\%$).

What should be noticed is that the GES component is more significant in the top right panel in Figure 4, where the stars are located with $4 < Z < 6 \text{ kpc}$, but this is not clear for the outer volumes with $12 < R < 20 \text{ kpc}$ in Figure 5. It is not clear that the *missing* of GES is intrinsic or that the larger uncertainties of the distances make the distribution of the action J_ϕ more diffused.

3.3. Rotational velocity distribution of the disk

Besides the halo component, the variances of the rotational velocity and its dispersion of the disk component are also obtained with the sample $[\text{Fe}/\text{H}] < -1$, even though this may not represent the whole typical thick disk. What should be noticed is that our model for the Bayesian method does not include the metal weak thick disk (Carollo et al. 2019) as a independent component, because of the low fraction in our sample.

From the top panels in Figure 2 which represent the results of S-sample, we find that the rotational velocity of the disk component (red symbols) decreases with increasing height to the disk plane, while the dispersion increases. As those stars with metallicity $[\text{Fe}/\text{H}] > -1$ are removed, there are too few thin disk stars are left in our sample (Hayden et al. 2015) to bring a significant offset. From Table 1, we find that the rotational velocity is around $185_{-5}^{+5} \text{ km s}^{-1}$ for

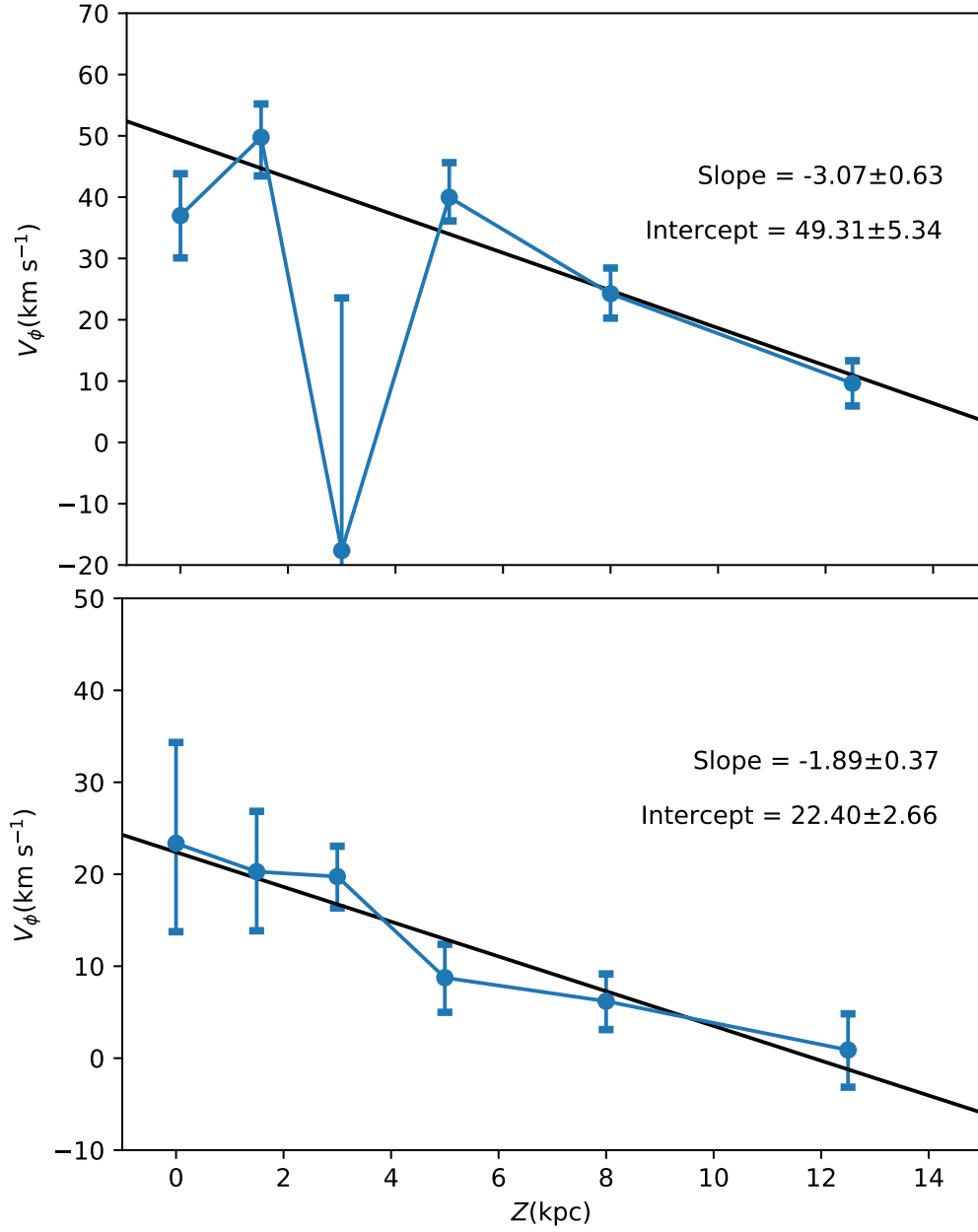


Figure 3. Rotational velocity distributions of the halo in the S-sample and SO-sample are shown versus the height to the disk in the left and right panels with the blue symbols, respectively. The solid black lines represent the regression linear relative. The parameters for the regression are marked on the top-right corner.

the volume $-1 < Z < 1$ kpc, which also suggests that it is contributed by the thick disk component (Morrison et al. 1990). It decreases to 127 km s^{-1} of the volume with $2 < Z < 4$ kpc for the S-sample. Meanwhile, the dispersion of the rotational velocity increases from 41 km s^{-1} at lowest volume to 55 km s^{-1} . The decreasing trend of the rotational velocity and the increasing trend of the rotational velocity dispersion support the conclusion of Liu & van de Ven (2012), that there may be two components of the thick disk.

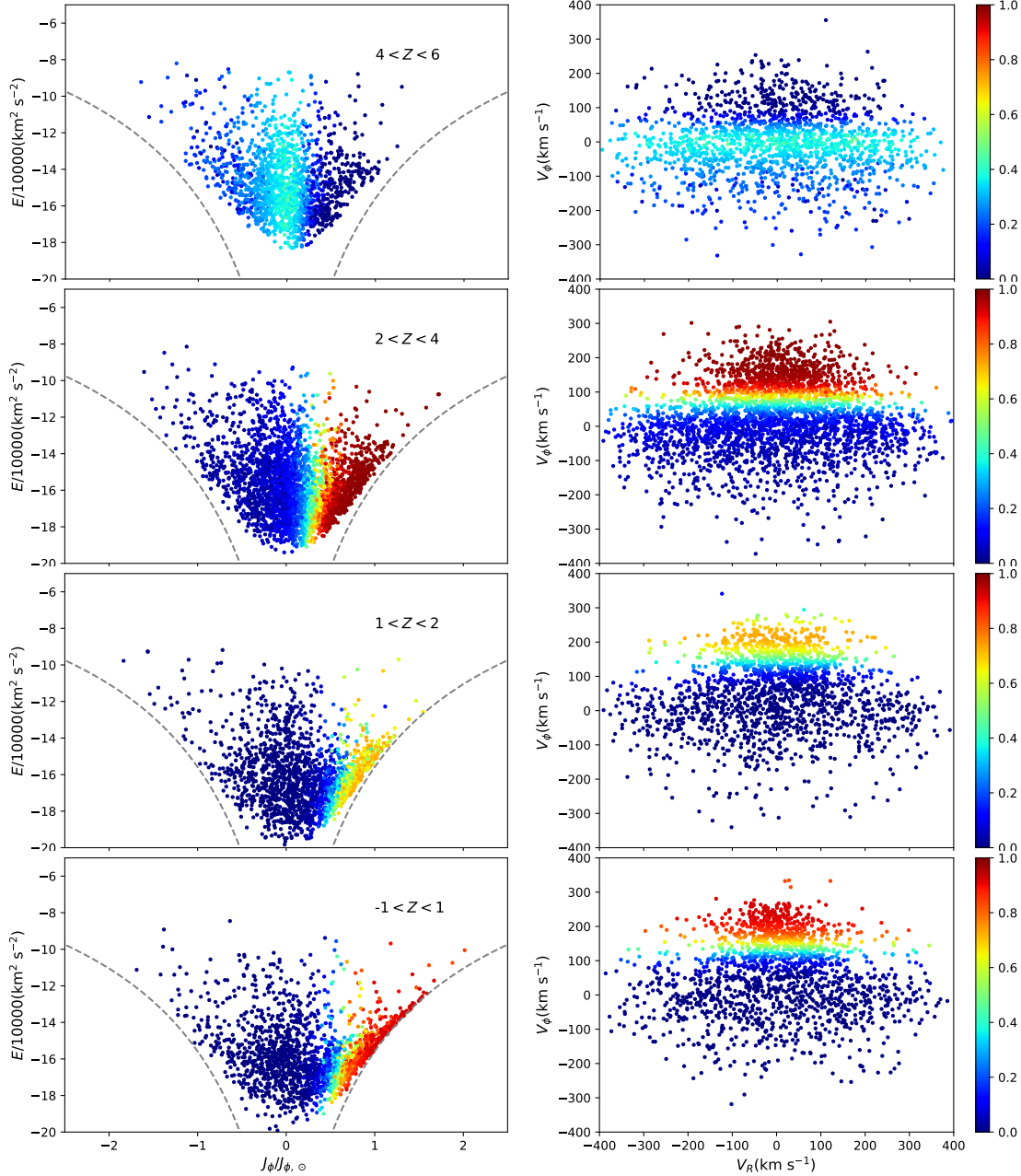


Figure 4. The phase space distributions of the stars in the different volumes from S-sample are shown. The left and right panels show the distribution in action J_ϕ versus energy E and velocity spaces, respectively. The stars are color-coded by the probability of belonging to the disk component for the volumes with $Z < 4$ kpc, or the probability of belonging to the GES component for the volume with $4 < Z < 6$ kpc. The dashed lines in the left panels represent the circular orbits. From top to the bottom, the panels represent the volumes with different height, e.g. $4 < Z < 6$ kpc, $2 < Z < 4$ kpc, $1 < Z < 2$ kpc, $-1 < Z < 1$ kpc, respectively.

Different with the results from the S-sample, the rotational velocity of the disk component in the SO-sample decreases firstly and becomes flat, around 200 km s^{-1} , at higher Z . The rotational velocity dispersion for SO-sample increases with the height to the disk plane from 20 km s^{-1} to 45 km s^{-1} .

Figures 4 and 5 show the distribution of the stars in $E - J_\phi$ and $V_\phi - V_R$ spaces, respectively. The stars are color-coded by the probability of belonging to the disk or the GES. We find that the disk stars with high probabilities (the red dots) in the SO-sample are much closer to the circular orbit line (the dashed line) than those in the S-sample. Comparing with the results from Li et al. (2012) and Xu et al. (2015), those stars of high probabilities to be disk members with

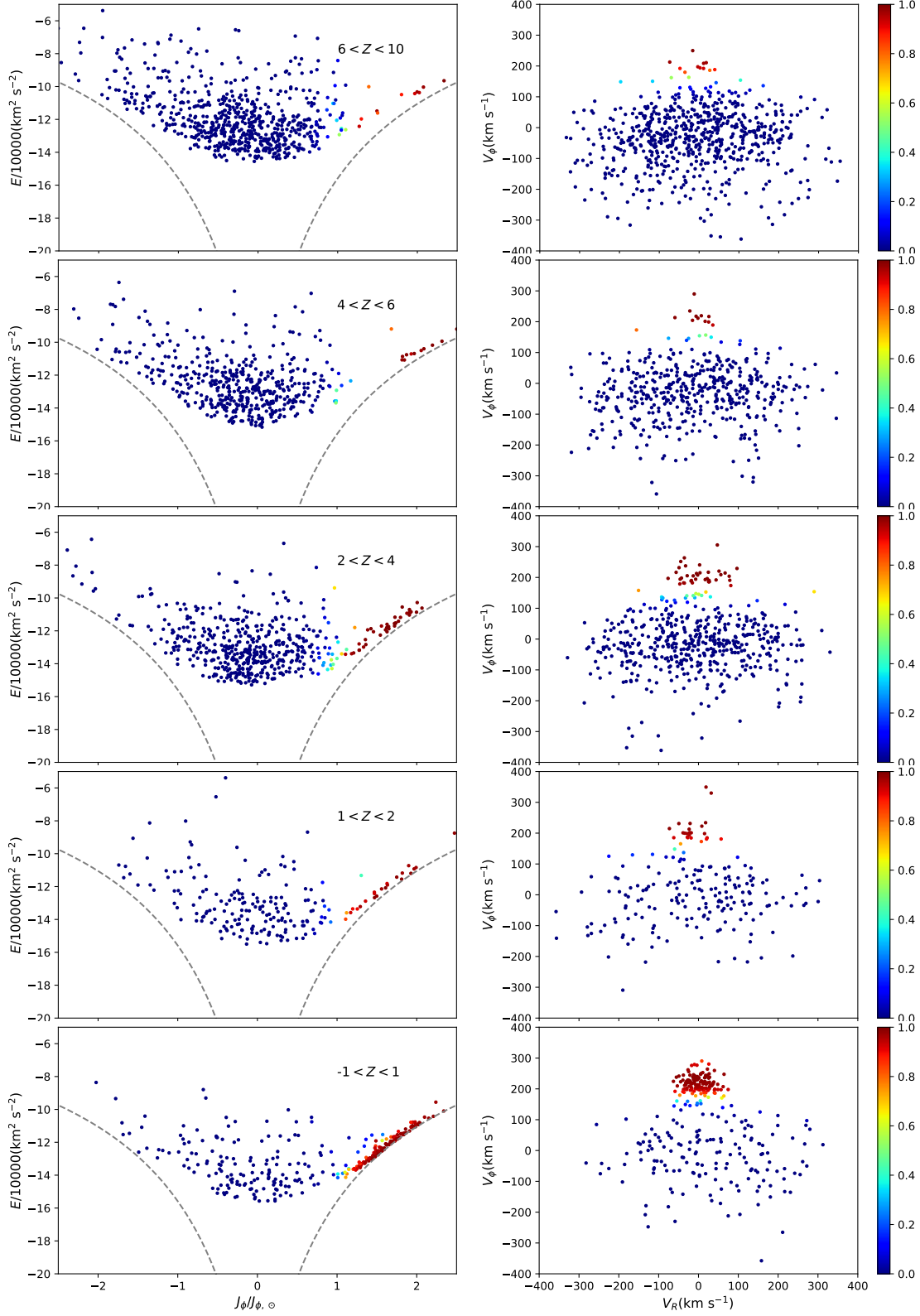


Figure 5. Similar to Figure 4, but for the stars from SO-sample. From top to the bottom, the panels represent the volumes with different heights, i.g. $6 < Z < 10$ kpc, $4 < Z < 6$ kpc, $2 < Z < 4$ kpc, $1 < Z < 2$ kpc, $-1 < Z < 1$ kpc, respectively. The dots are color-coded by the probability of belonging to the disk component.

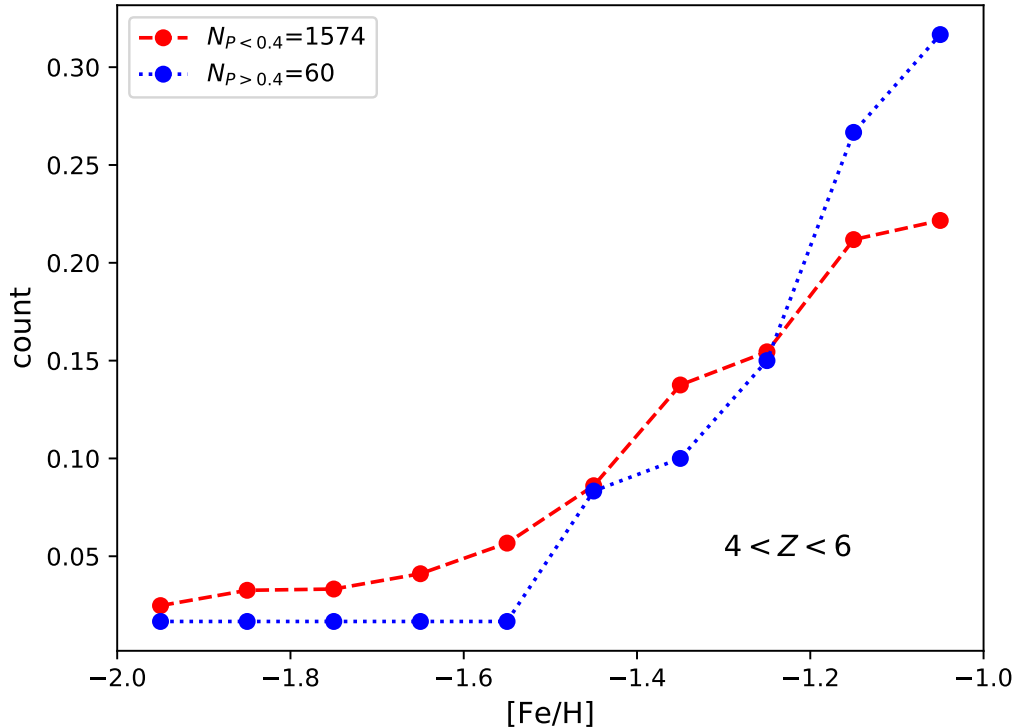


Figure 6. The histogram distribution of the metallicity of the stars with in the S-sample with $4 < Z < 6$ kpc. The distributions of the stars with probability higher and lower than 0.5 are represented with blue and red symbols, respectively.

rotational velocity of $\sim 200 \text{ km s}^{-1}$ overlap with the substructure Monoceros Ring. As claimed by Xu et al. (2015), the disk stars can be heated by the disk oscillations and reach to larger heights. So in this work, those stars with larger rotational velocities are possible the extension of the disk, which is also approved by Li et al (2020, in prep.), who analyse those Galactic Anticenter Substructures including the Monoceros Ring and the Triangulum-Andromeda cloud in dynamical and chemical spaces.

3.4. Disk Flare

The red symbols in the bottom panels of Figure 2 show the distributions of the disk for outer volumes with $12 < R < 20$ kpc. The green symbols represent the results with an additional component in the model. According to the rotational velocity and its dispersion, this component is an extension of the disk. In other words, the disk component extends to higher volumes up to $6 \sim 10$ kpc with galactocentric distance R between 12 and 20 kpc. This is also represented by the red symbols in Figure 5. That is the disk flare, that the outer disk is much thicker. This is also indicated with scale length distribution by Wang et al. (2018) using the same K giant sample.

4. DISCUSSION

4.1. Interaction between the halo and the disk

There are many mechanisms to generate the differential rotation of the halo. One possible mechanism for the decreasing trend of the halo rotational velocity versus the height to the disk plane is the interaction between the halo and the disk. In order to check this scenario, we use the simulated galaxies from the TNG100 simulation (Springel et al. 2018; Pillepich et al. 2018a; Marinacci et al. 2018; Naiman et al. 2018). The TNG 100 simulation is a magnetohydrodynamic cosmological simulation, which contains 2×1820^3 resolution elements in a cosmological in a $(110 \text{ Mpc})^3$ box. Compared with the original Illustris simulation (Vogelsberger et al. 2013; Torrey et al. 2014), the TNG simulation has adopted new physics models and improved the implementations of galactic winds, stellar evolution, chemical enrichment (Pillepich et al. 2018b), and AGN feedback (Weinberger et al. 2017). Therefore, the TNG simulation can reproduced many

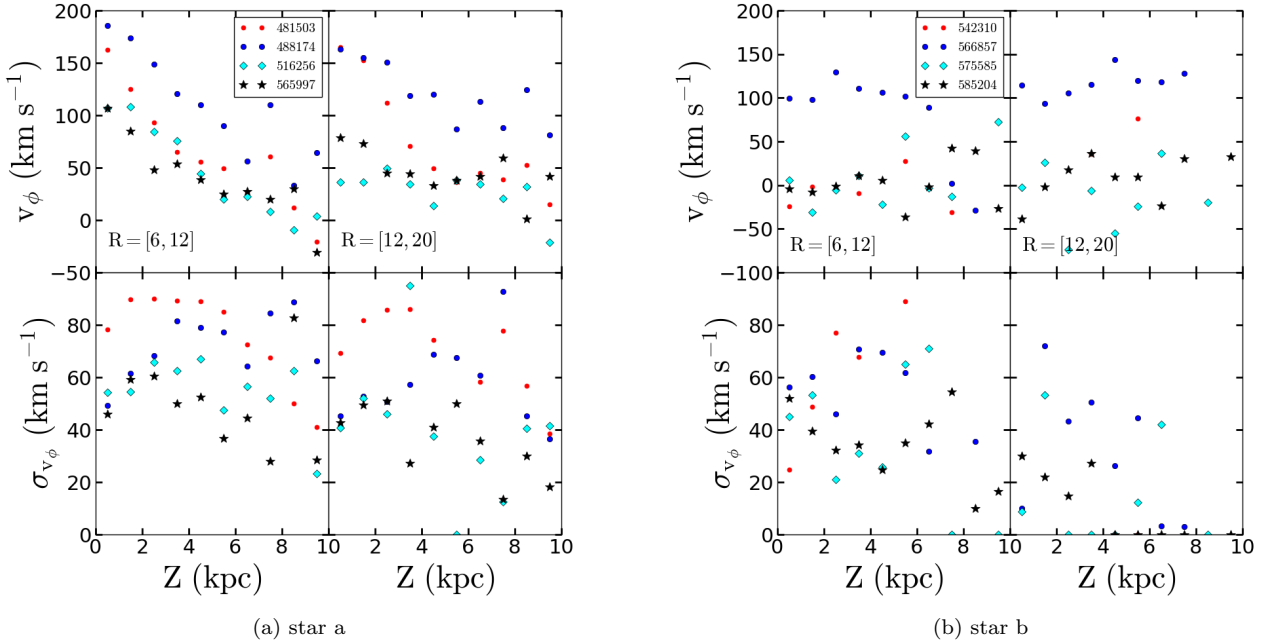


Figure 7. The velocity v_ϕ and velocity dispersion σ_{v_ϕ} distributions for eight galaxies. (a) the results of star particles for four galaxies, the axis ratios from the star particles for galaxy 481503, 488174, 516256 and 565997 are 1:0.997:0.213, 1:0.988:0.312, 1:0.988:0.432 and 1:0.995:0.325, respectively. (b) Same as panel (a), the results for galaxies 542310, 566857, 575585 and 585204. The axis ratio from the star particles for these galaxies are: 1:0.985:0.751, 1:0.982:0.749, 1:0.985:0.781 and 1:0.985:0.808, respectively.

observed galaxy properties better and scaling relations to different degrees. Galaxies in their host dark-matter halos were identified using the SUBFIND halo finding algorithm (Dolag et al. 2009). In Figure 7, we show the velocity v_ϕ and velocity dispersion σ_{v_ϕ} for eight galaxies from the TNG simulation with different axis ratios. It is seen that there are clear velocity gradients in v_ϕ for stars in the panel (a). For these four galaxies, they exist the oblate-disk, with the axis ratio c/a (minor axis over major axis) lower than 0.5. For the other four galaxies as shown in panels (b), the stellar systems are nearly spherical or triaxial, with $c/a > 0.5$, there are no obvious velocity gradients in v_ϕ versus height to the disk.

As shown in Wang et al. (2019), the oblate galaxies have larger spin parameters than prolate and triaxial galaxies. In other words, the oblate system has the larger rotational velocity. Close to the oblate-disk, the fast rotation disk dominates the rotation velocity. With the height increasing, the halo begins to dominate the kinematics of the system, and the halo is more spherical or triaxial. Therefore, v_ϕ decreases with the height to the disk. In other words, the decreasing trend of the halo versus the height to the disk is quite likely caused by the dynamical interaction between the disk and the halo. A stronger disk makes the larger decreasing rate. From the comparison, we confirm that the halo must be oblate, which is consistent with the conclusion of Xu et al. (2018).

4.2. Interaction between the halo and the bar

Our Milky Way is a typical barred galaxy and the bar can affect the redistribution of the angular momentum in the system. Angular momentum is emitted from the bar region and absorbed by the corotation resonance (hereafter CR) and outer Lindblad resonance (hereafter OLR) in the disk, and also absorbed in the spheroid components by all resonances (Athanasoula 2013). The pattern speed of the Milky Way bar is $40 \sim 60 \text{ km s}^{-1} \text{ kpc}^{-1}$ (Wang et al. 2012, 2013; Long et al. 2013; Portail et al. 2017), and the corresponding OLR radius is smaller than 8.5 kpc. In our SO-sample, we still find the clear rotational trend for the halo star, therefore, the effect from the bar is small for our findings here. In the other hand, the disk component can extend to the outer part, even as far as 20 kpc. This suggests the possibility for the disk to affect the halo spin (Valluri et al. 2012).

4.3. *The halo assemble history*

The third possibility for the rotation of the halo is the assemble history. Those merged satellites should have a random angular momentum distribution (Sanderson et al. 2015), unless that most of those satellites fall in groups and those groups dominating the inner halo, such as the GES (Helmi et al. 2018; Belokurov et al. 2018) and *Sequoia* (Myeong et al. 2019). As we discussed above, we treat the GES as a different component in the model. Meanwhile, the *Sequoia* has a very retrograde rotational velocity. The possibility is too low to lead a decreasing trend for the rotational velocity versus the height.

4.4. *The dichotomy of the halo*

Another possible explanation for the decreasing trend is the dichotomy of the halo. Carollo et al. (2007) found that the inner and the outer part of the halo have different chemical and dynamic properties. The dichotomy were confirmed by Fernández-Alvar et al. (2015) and Yoon et al. (2018) with abundance distributions of calcium, magnesium and carbon. According to the results of conclusion of Carollo et al. (2007), the inner halo rotates progradely with a modest speed. In contrast, the outer part is retrogradely rotating. An et al. (2013) also found the similar results, that the retrogradely rotating stars are generally more metal poor.

Considering the large overlapping of the inner and outer halo and their different rotation behavior Carollo et al. (2007), it is possible to bring a decreasing trend of the rotational velocity versus the height to the disk plane in the transition region of the two halo. As the contribution of the inner halo decreases with a higher volume and the rotational velocity of the complex will decrease. Surprisingly, as showed in Figure 3, the trend in the S-sample is significantly steeper than that in the SO-sample. This suggests that the decreasing trend in the SO-sample may be caused by the dichotomy of the halo, but that in the S-sample is not mainly caused by the dichotomy of the halo, at least this may not be the main reason. This is also supported by the rotational velocity dispersion distribution. As showed in Figure 2, the dispersion in the S-sample is almost flat, which suggests that the inner halo is dominating. Meanwhile the variance of the rotational velocity dispersion is changing significantly for the SO-sample. It indicates that the dichotomy of the halo plays an important role to generate the decreasing trend in the SO-sample.

Above all, we claim that the dichotomy of the halo plays an important role in generating the decreasing trend of the rotational velocity distribution in the SO-sample, but this is not the main mechanism for the decreasing trend in the S-sample.

4.5. *Effect of the distance calculation*

To figure out if the rotational velocity distribution will be affected by the distance calculation, we firstly redo the procedures with different distance correction coefficients. Based on the previous distance correction, we multiply an additional coefficient to the corrected distance, e.g. 0.9 and 1.1. After all the same steps, we find that, the rotational velocity decreasing trend for the halo component is still there, but the decreasing rate (the slope) varies slightly, from $-3.03 \pm 0.73 \text{ km s}^{-1} \text{ kpc}^{-1}$ to $-3.79 \pm 0.97 \text{ km s}^{-1} \text{ kpc}^{-1}$ for inner volumes with coefficients of 0.9 and 1.1, respectively. Meanwhile for the outer volumes the decreasing rate varies from $-2.06 \pm 0.46 \text{ km s}^{-1} \text{ kpc}^{-1}$ to $-1.30 \pm 0.37 \text{ km s}^{-1} \text{ kpc}^{-1}$ with the coefficients of 0.9 and 1.1, respectively. That means the rotational velocity gradient is intrinsic, and the gradient for the outer volume is a bit shallower.

5. SUMMARY

We use the K-giant stars from LAMOST DR5 to investigate the rotation information of the halo and the disk. We find that the rotational velocity of the halo decreases with an increasing height to the disk plane. The dispersion of the halo is almost flat up to 15 kpc. The rotational velocity of the inner part decreases faster than that of the outer part, -2.75 and $-1.88 \text{ km s}^{-1} \text{ kpc}^{-1}$ respectively. Analysing all the possible mechanisms for the decreasing trend, we claim that the decreasing trend suggests an oblate halo profile, which is consistent with that revealed by Xu et al. (2018). This is possibly caused by the interaction between the halo and the disk component.

The signal of merging event GES is clear shown only in the volumes with height from 2 to 10 kpc and galactocentric distance between 6 and 12 kpc. Meanwhile the rotational velocity dispersion of the disk is larger in higher volumes. At the same time, the rotational velocity decreases versus the height. Our results also show a flaring disk, which can reach the height of 6 to 10 kpc with galactocentric distance from 12 to 20 kpc. Limited by the sample, we claim that the disk can reach at least 20 kpc.

In order to avoid the contamination of different components, we use the Bayesian method to determine the rotational velocity for each component at different locations statistically. With the rotational velocity distribution of each

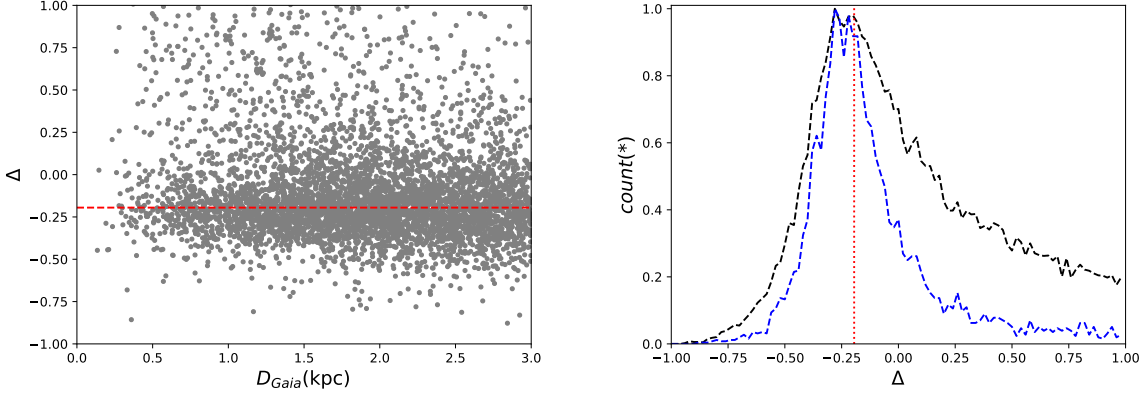


Figure 8. Left panel: The distribution of the distance difference Δ is shown versus the Gaia distance D_{Gaia} with the gray dots. Right panel: The histogram distribution of the distance difference Δ is shown. The black line represents the distribution of the whole sample while the blue line represents the distribution of the stars with reliable Gaia distances and high signal-to-noise ratios during LAMOST observation. The red lines in both panel represent the value for the distance correction.

component, it is able to determine the probability for each star belonging to the different components. As showed in Figures 4 and 5, only the disk component can be well picked out. The GES and the halo are still difficult to separate. This will be improved in future for member stars selection of the two components using the full phase space information. More purer samples will greatly help the chemical studies in future with spectral data sets from LAMOST (Liu et al. 2020), SEGUE (Yanny et al. 2009) and APOGEE (Majewski et al. 2017).

APPENDIX

A. DISTANCE CORRECTION

To make sure the distances from Gaia DR2 and LAMOST are consistent, we firstly select the common K-giant stars in both Gaia DR2 and LAMOST DR5 with following criteria,

- $\omega/\omega_{err} > 5$
- $D_{Gaia} < 3$ kpc
- $\sigma_{D_{Gaia}}/D_{Gaia} < 0.1$
- $SNR > 10$

The first criterion is used to select those stars with parallaxes are well measured. The second and the third ones are used to constrain the distance D_{Gaia} smaller than 3 kpc and high accuracy, which is provided by Bailer-Jones et al. (2018). The last item is used to constrain the data from LAMOST DR5 with high signal-to-noise ratio. After the selection, we have 5560 K-giant stars with distance accurately measured by Gaia and reliable spectra from LAMOST DR5.

To compare the distances we define the difference $\Delta = \frac{D_L - D_{Gaia}}{D_{Gaia}}$, where D_L is the distance provided by Liu et al. (2014), and D_{Gaia} is the distance from Bailer-Jones et al. (2018).

Figure 8 shows the distribution of the distance difference versus the Gaia distance D_{Gaia} in the left panel and its histogram distribution in the right panel. From the distribution we can find that there is a system offset with Δ a constant around -0.2. To obtain the true value, we calculate the mean value of Δ and its dispersion, $\langle \Delta \rangle$ and σ_Δ , and then select those stars within $1\sigma_\Delta$. Iterating this step until the mean value does not change significantly, lower than 0.005. The threshold is chosen because with this value the distance system error will be lower than 0.15 kpc at 30 kpc. Finally, we obtain the value $\Delta \sim -0.195$, as shown by the red line in both of the panels in Figure 8. In this case, the distance from LAMOST DR5 is corrected by dividing 0.805. Figure 9 shows the corrected LAMOST distance distribution as a function of the Gaia distance D_{Gaia} . The red line represents the 1:1 relation.

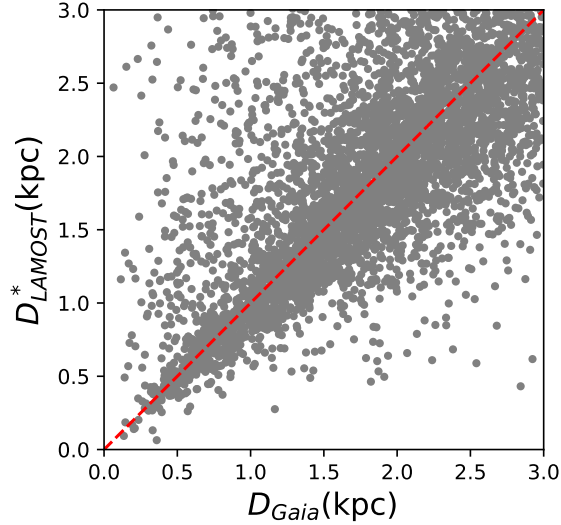


Figure 9. The relation between the corrected LAMOST distance D_{LAMOST}^* and Gaia distance D_{Gaia} is shown. The red line represents the distance ratio 1:1.

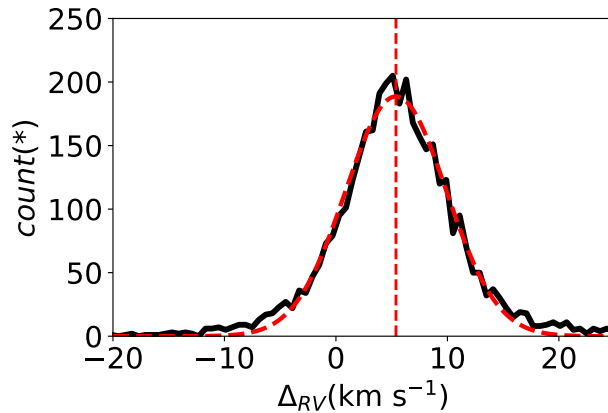


Figure 10. The radial velocity comparison between the values from LAMOST DR5 and GDR2. The red dashed line represent the fitting results with one Gaussian model, with mean value at ~ 5.38 km s⁻¹ and a dispersion 6.39 km s⁻¹.

B. RADIAL VELOCITY CORRECTION

The radial velocity provided by GDR2 is only available for bright stars with $G < 14$. That will cause the sample cannot trace distant volumes. In this paper we adopt the radial velocity from LAMOST DR5. Figure 10 shows the comparison between the radial velocities provided by LAMOST DR5 and GDR2 of the common K-giant stars used in Paper I. We can clearly find an offset of ~ 5.38 km s⁻¹ and a dispersion 6.39 km s⁻¹. In this paper, we correct the radial velocity from LAMOST DR5 with $+5.38$ km s⁻¹.

C. PARAMETER DETERMINATION IN BAYESIAN METHOD

We adopt the median values for each parameter during the Bayesian method from *emcee*. The upper and lower uncertainties are determined as the difference between the median value and the 84% and 16% values. Figure 11 shows the corner distribution of the possible values for each parameter. The blue lines represent the median values for each parameter, while the dashed lines in each histogram distribution represent the 16%, 50% and 84% values. Figure 12 shows the fitting results of the rotational velocity distribution. The red and green dashed lines represent the halo and disk components, respectively. The vertical cyan dashed line represent the rotational velocity 0.

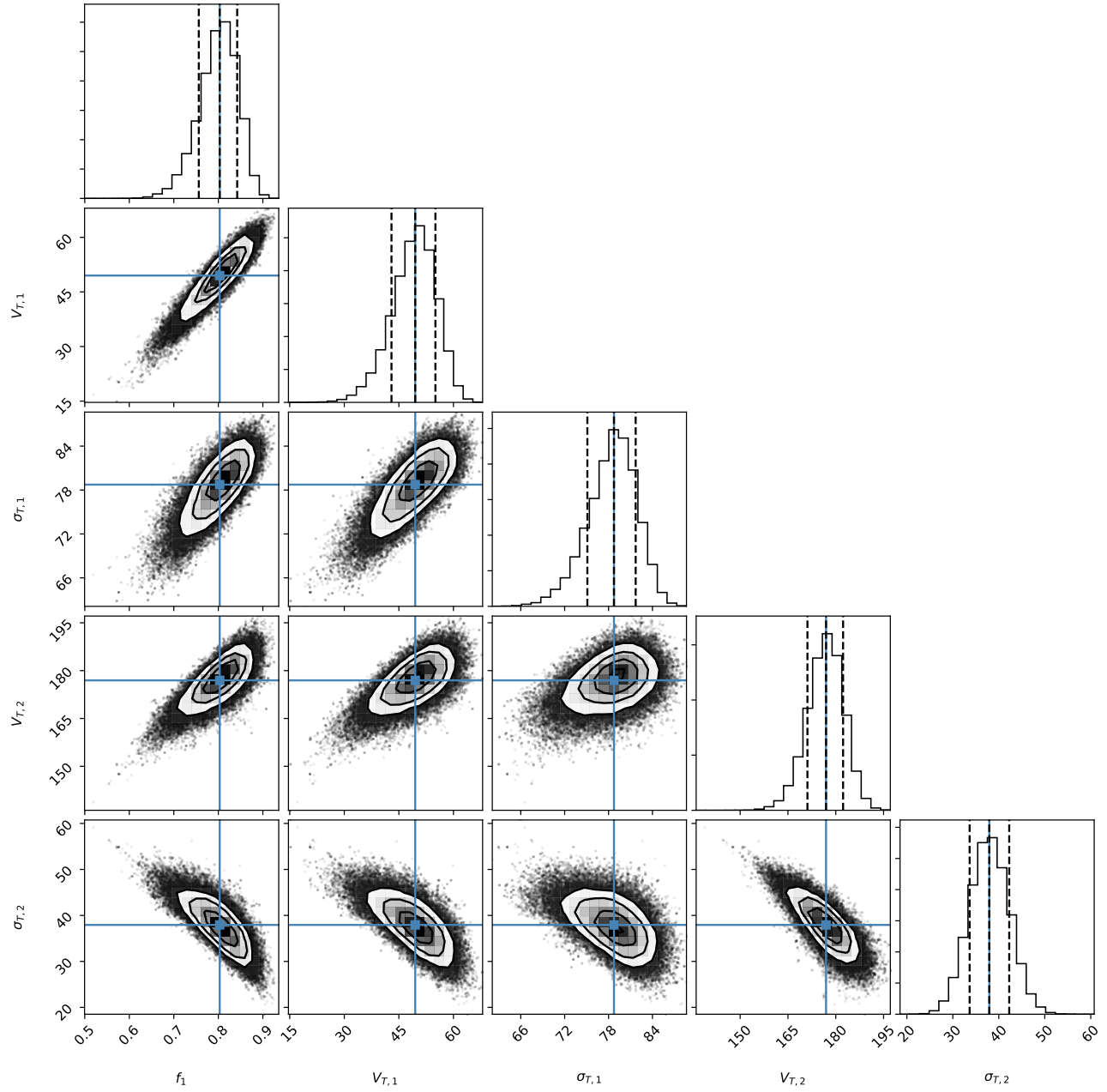


Figure 11. Results from Bayesian method is showed for the volume with $1 < Z < 2$ kpc in S-sample. The dashed lines indicate the 16%, 50% and 84% values for each parameter. The blue solid lines represent the median values for the parameters which are adopted for the components.

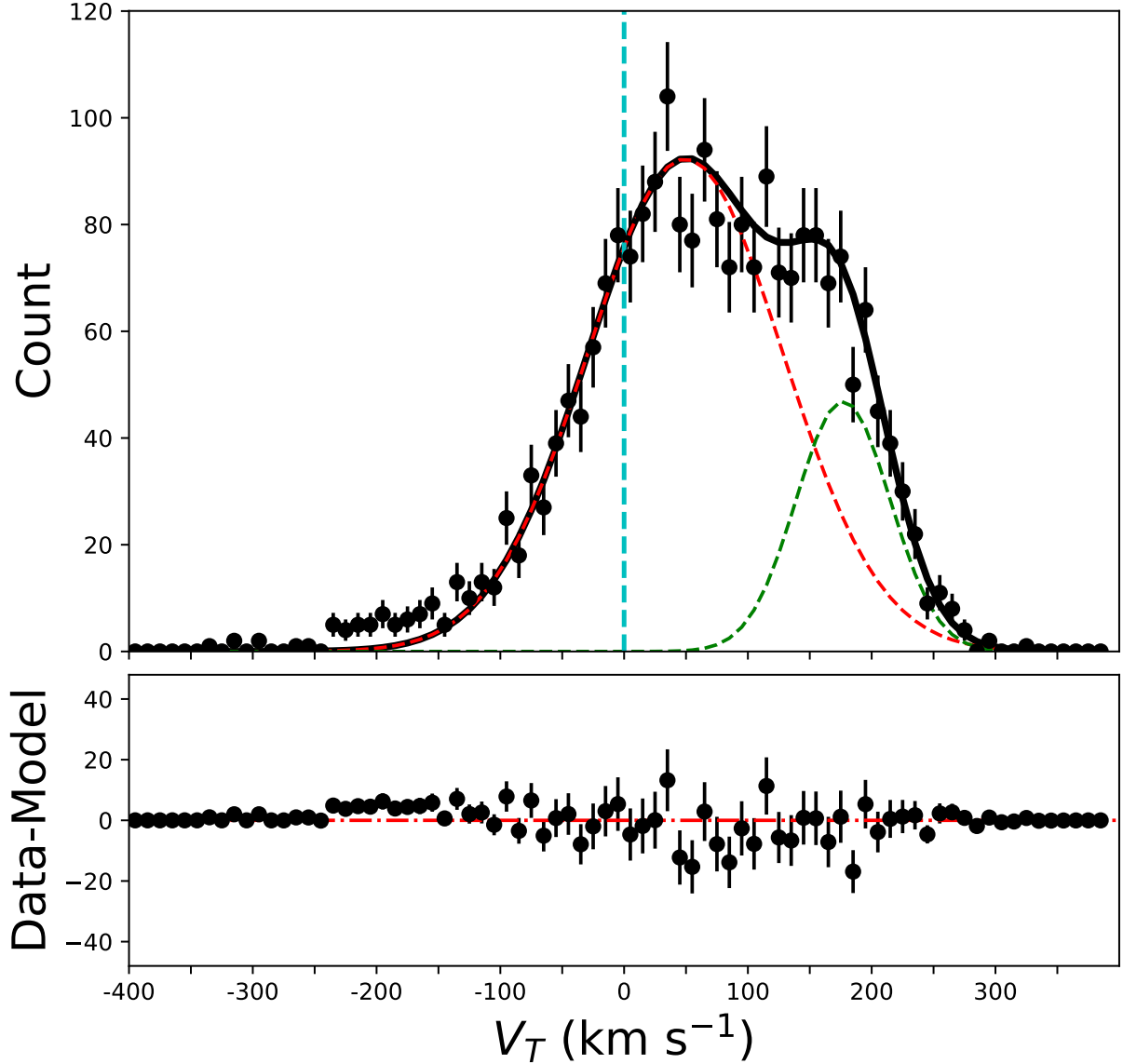


Figure 12. Top panel: The black dots indicate the histogram distribution of the rotational velocity. The red and green dashed lines represent the distributions of the halo and disk components in the model defined during the Bayesian method, respectively. The solid black line represents the distribution of all the stars constrained by the Bayesian method. The cyan vertical line indicates the value 0 for the rotational velocity and model. Bottom panel: the residual distribution between the histogram distribution of the observational rotational velocity and model.

ACKNOWLEDGMENTS

We thank Lia Athanassoula and Victor Debattista for helpful discussions. This work is supported by National Key R&D Program of China No. 2019YFA0405500. C.L. thanks the National Natural Science Foundation of China (NSFC) with grant No. 11835057. Y.W. thanks the National Natural Science Foundation of China (NSFC) with grant No. 11773034. X.-X. Xue thanks the support of NSFC under grants No. 11873052 and No. 11890694. The LAMOST FELLOWSHIP is supported by Special Funding for Advanced Users, budgeted and administrated by Center for Astronomical Mega-Science, Chinese Academy of Sciences (CAMS). This work is supported by Cultivation Project for LAMOST Scientific Payoff and Research Achievement of CAMS-CAS.

Guoshoujing Telescope (the Large Sky Area Multi-Object Fiber Spectroscopic Telescope LAMOST) is a National Major Scientific Project built by the Chinese Academy of Sciences. Funding for the project has been provided by the National Development and Reform Commission. LAMOST is operated and managed by the National Astronomical Observatories, Chinese Academy of Sciences. This work has made use of data from the European Space Agency (ESA) mission *Gaia* (<https://www.cosmos.esa.int/gaia>), processed by the *Gaia* Data Processing and Analysis Consortium (DPAC, <https://www.cosmos.esa.int/web/gaia/dpac/consortium>). Funding for the DPAC has been provided by national institutions, in particular the institutions participating in the *Gaia* Multilateral Agreement.

Software: astropy (Astropy Collaboration et al. 2013),
Galpy (Bovy 2015),
emcee (Foreman-Mackey et al. 2013)

REFERENCES

- An, D., Beers, T. C., Johnson, J. A., et al. 2013, *ApJ*, 763, 65, doi: [10.1088/0004-637X/763/1/65](https://doi.org/10.1088/0004-637X/763/1/65)
- Antoja, T., Helmi, A., Romero-Gómez, M., et al. 2018, *Nature*, 561, 360, doi: [10.1038/s41586-018-0510-7](https://doi.org/10.1038/s41586-018-0510-7)
- Astropy Collaboration, Robitaille, T. P., Tollerud, E. J., et al. 2013, *A&A*, 558, A33, doi: [10.1051/0004-6361/201322068](https://doi.org/10.1051/0004-6361/201322068)
- Athanassoula, E. 2013, Bars and secular evolution in disk galaxies: Theoretical input, ed. J. Falcón-Barroso & J. H. Knapen, 305
- Bailer-Jones, C. A. L., Rybizki, J., Fouesneau, M., Mantelet, G., & Andrae, R. 2018, *AJ*, 156, 58, doi: [10.3847/1538-3881/aacb21](https://doi.org/10.3847/1538-3881/aacb21)
- Belokurov, V., Erkal, D., Evans, N. W., Koposov, S. E., & Deason, A. J. 2018, *MNRAS*, 478, 611, doi: [10.1093/mnras/sty982](https://doi.org/10.1093/mnras/sty982)
- Belokurov, V., Sanders, J. L., Fattahi, A., et al. 2019, arXiv e-prints, arXiv:1909.04679, <https://arxiv.org/abs/1909.04679>
- Bernard, E. J., Ferguson, A. M. N., Schlafly, E. F., et al. 2016, *MNRAS*, 463, 1759, doi: [10.1093/mnras/stw2134](https://doi.org/10.1093/mnras/stw2134)
- Bird, S. A., Xue, X.-X., Liu, C., et al. 2019, *AJ*, 157, 104, doi: [10.3847/1538-3881/aafd2e](https://doi.org/10.3847/1538-3881/aafd2e)
- Bland-Hawthorn, J., & Gerhard, O. 2016, *ARA&A*, 54, 529, doi: [10.1146/annurev-astro-081915-023441](https://doi.org/10.1146/annurev-astro-081915-023441)
- Bovy, J. 2015, *ApJS*, 216, 29, doi: [10.1088/0067-0049/216/2/29](https://doi.org/10.1088/0067-0049/216/2/29)
- Carlin, J. L., Liu, C., Newberg, H. J., et al. 2015, *AJ*, 150, 4, doi: [10.1088/0004-6256/150/1/4](https://doi.org/10.1088/0004-6256/150/1/4)
- Carollo, D., Beers, T. C., Lee, Y. S., et al. 2007, *Nature*, 450, 1020, doi: [10.1038/nature06460](https://doi.org/10.1038/nature06460)
- Carollo, D., Chiba, M., Ishigaki, M., et al. 2019, *ApJ*, 887, 22, doi: [10.3847/1538-4357/ab517c](https://doi.org/10.3847/1538-4357/ab517c)
- Dierickx, M. I. P., & Loeb, A. 2017, *ApJ*, 836, 92, doi: [10.3847/1538-4357/836/1/92](https://doi.org/10.3847/1538-4357/836/1/92)
- Dolag, K., Borgani, S., Murante, G., & Springel, V. 2009, *MNRAS*, 399, 497, doi: [10.1111/j.1365-2966.2009.15034.x](https://doi.org/10.1111/j.1365-2966.2009.15034.x)
- Fernández-Alvar, E., Allende Prieto, C., Schlesinger, K. J., et al. 2015, *A&A*, 577, A81, doi: [10.1051/0004-6361/201425455](https://doi.org/10.1051/0004-6361/201425455)
- Foreman-Mackey, D., Hogg, D. W., Lang, D., & Goodman, J. 2013, *PASP*, 125, 306, doi: [10.1086/670067](https://doi.org/10.1086/670067)
- Gaia Collaboration, Prusti, T., de Bruijne, J. H. J., et al. 2016, *A&A*, 595, A1, doi: [10.1051/0004-6361/201629272](https://doi.org/10.1051/0004-6361/201629272)
- Gaia Collaboration, Brown, A. G. A., Vallenari, A., et al. 2018a, *A&A*, 616, A1, doi: [10.1051/0004-6361/201833051](https://doi.org/10.1051/0004-6361/201833051)
- Gaia Collaboration, Katz, D., Antoja, T., et al. 2018b, *A&A*, 616, A11, doi: [10.1051/0004-6361/201832865](https://doi.org/10.1051/0004-6361/201832865)
- Grillmair, C. J., & Dionatos, O. 2006a, *ApJL*, 641, L37, doi: [10.1086/503744](https://doi.org/10.1086/503744)
- . 2006b, *ApJL*, 643, L17, doi: [10.1086/505111](https://doi.org/10.1086/505111)
- Hayden, M. R., Bovy, J., Holtzman, J. A., et al. 2015, *ApJ*, 808, 132, doi: [10.1088/0004-637X/808/2/132](https://doi.org/10.1088/0004-637X/808/2/132)
- Helmi, A., Babusiaux, C., Koppelman, H. H., et al. 2018, *Nature*, 563, 85, doi: [10.1038/s41586-018-0625-x](https://doi.org/10.1038/s41586-018-0625-x)
- Hernitschek, N., Cohen, J. G., Rix, H.-W., et al. 2018, *ApJ*, 859, 31, doi: [10.3847/1538-4357/aabfbb](https://doi.org/10.3847/1538-4357/aabfbb)
- Ibata, R. A., Bellazzini, M., Malhan, K., Martin, N., & Bianchini, P. 2019, *Nature Astronomy*, 3, 667, doi: [10.1038/s41550-019-0751-x](https://doi.org/10.1038/s41550-019-0751-x)
- Ibata, R. A., Gilmore, G., & Irwin, M. J. 1994, *Nature*, 370, 194, doi: [10.1038/370194a0](https://doi.org/10.1038/370194a0)
- Laporte, C. F. P., Minchev, I., Johnston, K. V., & Gómez, F. A. 2019, *MNRAS*, 485, 3134, doi: [10.1093/mnras/stz583](https://doi.org/10.1093/mnras/stz583)
- Law, D. R., & Majewski, S. R. 2010, *ApJ*, 714, 229, doi: [10.1088/0004-637X/714/1/229](https://doi.org/10.1088/0004-637X/714/1/229)
- Li, J., Newberg, H. J., Carlin, J. L., et al. 2012, *ApJ*, 757, 151, doi: [10.1088/0004-637X/757/2/151](https://doi.org/10.1088/0004-637X/757/2/151)
- Liu, C., & van de Ven, G. 2012, *MNRAS*, 425, 2144, doi: [10.1111/j.1365-2966.2012.21551.x](https://doi.org/10.1111/j.1365-2966.2012.21551.x)
- Liu, C., Deng, L.-C., Carlin, J. L., et al. 2014, *ApJ*, 790, 110, doi: [10.1088/0004-637X/790/2/110](https://doi.org/10.1088/0004-637X/790/2/110)

- Liu, C., Fu, J., Shi, J., et al. 2020, arXiv e-prints, arXiv:2005.07210. <https://arxiv.org/abs/2005.07210>
- Long, R. J., Mao, S., Shen, J., & Wang, Y. 2013, MNRAS, 428, 3478, doi: [10.1093/mnras/sts285](https://doi.org/10.1093/mnras/sts285)
- Lux, H., Read, J. I., Lake, G., & Johnston, K. V. 2013, MNRAS, 436, 2386, doi: [10.1093/mnras/stt1744](https://doi.org/10.1093/mnras/stt1744)
- Majewski, S. R., Schiavon, R. P., Frinchaboy, P. M., et al. 2017, AJ, 154, 94, doi: [10.3847/1538-3881/aa784d](https://doi.org/10.3847/1538-3881/aa784d)
- Marinacci, F., Vogelsberger, M., Pakmor, R., et al. 2018, MNRAS, 480, 5113, doi: [10.1093/mnras/sty2206](https://doi.org/10.1093/mnras/sty2206)
- Morrison, H. L., Flynn, C., & Freeman, K. C. 1990, AJ, 100, 1191, doi: [10.1086/115587](https://doi.org/10.1086/115587)
- Myeong, G. C., Vasiliev, E., Iorio, G., Evans, N. W., & Belokurov, V. 2019, MNRAS, 488, 1235, doi: [10.1093/mnras/stz1770](https://doi.org/10.1093/mnras/stz1770)
- Naiman, J. P., Pillepich, A., Springel, V., et al. 2018, MNRAS, 477, 1206, doi: [10.1093/mnras/sty618](https://doi.org/10.1093/mnras/sty618)
- Pillepich, A., Nelson, D., Hernquist, L., et al. 2018a, MNRAS, 475, 648, doi: [10.1093/mnras/stx3112](https://doi.org/10.1093/mnras/stx3112)
- Pillepich, A., Springel, V., Nelson, D., et al. 2018b, MNRAS, 473, 4077, doi: [10.1093/mnras/stx2656](https://doi.org/10.1093/mnras/stx2656)
- Portail, M., Gerhard, O., Wegg, C., & Ness, M. 2017, MNRAS, 465, 1621, doi: [10.1093/mnras/stw2819](https://doi.org/10.1093/mnras/stw2819)
- Reid, M. J., Menten, K. M., Brunthaler, A., et al. 2014, ApJ, 783, 130, doi: [10.1088/0004-637X/783/2/130](https://doi.org/10.1088/0004-637X/783/2/130)
- Rodriguez-Gomez, V., Sales, L. V., Genel, S., et al. 2017, MNRAS, 467, 3083, doi: [10.1093/mnras/stx305](https://doi.org/10.1093/mnras/stx305)
- Sanderson, R. E., Helmi, A., & Hogg, D. W. 2015, ApJ, 801, 98, doi: [10.1088/0004-637X/801/2/98](https://doi.org/10.1088/0004-637X/801/2/98)
- Schönrich, R., & Aumer, M. 2017, MNRAS, 472, 3979, doi: [10.1093/mnras/stx2189](https://doi.org/10.1093/mnras/stx2189)
- Schönrich, R., Binney, J., & Dehnen, W. 2010, MNRAS, 403, 1829, doi: [10.1111/j.1365-2966.2010.16253.x](https://doi.org/10.1111/j.1365-2966.2010.16253.x)
- Springel, V., Pakmor, R., Pillepich, A., et al. 2018, MNRAS, 475, 676, doi: [10.1093/mnras/stx3304](https://doi.org/10.1093/mnras/stx3304)
- Thomas, G. F., McConnachie, A. W., Ibata, R. A., et al. 2018, MNRAS, 481, 5223, doi: [10.1093/mnras/sty2604](https://doi.org/10.1093/mnras/sty2604)
- Tian, H., Liu, C., Xu, Y., & Xue, X. 2019, ApJ, 871, 184, doi: [10.3847/1538-4357/aaf6e8](https://doi.org/10.3847/1538-4357/aaf6e8)
- Tian, H.-J., Liu, C., Carlin, J. L., et al. 2015, ApJ, 809, 145, doi: [10.1088/0004-637X/809/2/145](https://doi.org/10.1088/0004-637X/809/2/145)
- Torrey, P., Vogelsberger, M., Genel, S., et al. 2014, MNRAS, 438, 1985, doi: [10.1093/mnras/stt2295](https://doi.org/10.1093/mnras/stt2295)
- Valluri, M., Debattista, V. P., Quinn, T. R., Roškar, R., & Wadsley, J. 2012, MNRAS, 419, 1951, doi: [10.1111/j.1365-2966.2011.19853.x](https://doi.org/10.1111/j.1365-2966.2011.19853.x)
- Vera-Ciro, C., & Helmi, A. 2013, ApJL, 773, L4, doi: [10.1088/2041-8205/773/1/L4](https://doi.org/10.1088/2041-8205/773/1/L4)
- Vogelsberger, M., Genel, S., Sijacki, D., et al. 2013, MNRAS, 436, 3031, doi: [10.1093/mnras/stt1789](https://doi.org/10.1093/mnras/stt1789)
- Wang, H.-F., Liu, C., Xu, Y., Wan, J.-C., & Deng, L. 2018, MNRAS, 478, 3367, doi: [10.1093/mnras/sty1058](https://doi.org/10.1093/mnras/sty1058)
- Wang, Y., Mao, S., Li, H., et al. 2019, MNRAS, 483, 3048, doi: [10.1093/mnras/sty3297](https://doi.org/10.1093/mnras/sty3297)
- Wang, Y., Mao, S., Long, R. J., & Shen, J. 2013, MNRAS, 435, 3437, doi: [10.1093/mnras/stt1537](https://doi.org/10.1093/mnras/stt1537)
- Wang, Y., Zhao, H., Mao, S., & Rich, R. M. 2012, MNRAS, 427, 1429, doi: [10.1111/j.1365-2966.2012.22063.x](https://doi.org/10.1111/j.1365-2966.2012.22063.x)
- Weinberger, R., Springel, V., Hernquist, L., et al. 2017, MNRAS, 465, 3291, doi: [10.1093/mnras/stw2944](https://doi.org/10.1093/mnras/stw2944)
- Xu, Y., Newberg, H. J., Carlin, J. L., et al. 2015, ApJ, 801, 105, doi: [10.1088/0004-637X/801/2/105](https://doi.org/10.1088/0004-637X/801/2/105)
- Xu, Y., Liu, C., Xue, X.-X., et al. 2018, MNRAS, 473, 1244, doi: [10.1093/mnras/stx2361](https://doi.org/10.1093/mnras/stx2361)
- Xue, X. X., Rix, H. W., Zhao, G., et al. 2008, ApJ, 684, 1143, doi: [10.1086/589500](https://doi.org/10.1086/589500)
- Yanny, B., Rockosi, C., Newberg, H. J., et al. 2009, AJ, 137, 4377, doi: [10.1088/0004-6256/137/5/4377](https://doi.org/10.1088/0004-6256/137/5/4377)
- Yoon, J., Beers, T. C., Dietz, S., et al. 2018, ApJ, 861, 146, doi: [10.3847/1538-4357/aacceca](https://doi.org/10.3847/1538-4357/aacceca)
- York, D. G., Adelman, J., Anderson, John E., J., et al. 2000, AJ, 120, 1579, doi: [10.1086/301513](https://doi.org/10.1086/301513)